Active Shock Control in a Transonic Flow

Abraham. N. Gissen [*], Bojan Vukasinovic [*], Ari Glezer[*], and Sivaram P. Gogineni[†]

[*]Woodruff School of Mechanical Engineering, Georgia Institute of Technology, Atlanta, GA 30332-0405.
[†] Spectral Energies, 5100 Springfield Street, Suite 301, Dayton, OH 45431.

The control authority of fluidic actuation on a transonic shock and the induced adjacent separated flow domain are characterized over a two-dimensional convex surface in wind tunnel experiments. The shock is manipulated *indirectly* by controlling the induced separated flow downstream. Actuation is applied using a spanwise array of small-scale, high-frequency (nominally 10 kHz) fluidic oscillating jets that effect separation delay by enhancing small-scale mixing within the separating shear layer. This actuation approach enables control of both the shock position and suppression of its unsteady oscillation. The effects of the actuation amplitude are assessed using measurements of the static and dynamic surface pressure and PIV measurements. In addition, the correlation between the shock displacement and surface pressure are explored for application of closed-loop control of the shock.

Nomenclature

C_p	=	Pressure coefficient
C_q	=	Control mass flow rate coefficient
C_μ	=	Control momentum coefficient
f_d	=	Flow control frequency
H	=	Ramp height
M	=	Mach number
p_d	=	Dynamic downstream pressure
p_e	=	Static pressure at the test section end
p_i	=	Static pressure upstream from the test section
$p_k, k=1\text{-}15$	=	Static centerline pressures
p_{ref}	=	Static reference pressure
p_u	=	Dynamic upstream pressure
U	=	Mean streamwise velocity component
V	=	Mean cross-stream velocity component
ζ_{px}	=	Cross-correlation between p_d and the shock position

I. Background

Compressibility effects, and, in particular, the appearance of shock waves in transonic and supersonic flows can lead to significant penalties in the performance of external (airframes) and internal (propulsion) aerodynamic systems. Shock wave boundary layer interactions (SWBLIs) have been associated with local, and sometimes global flow separation, and pronounced unsteadiness with significant energy and performance losses (e.g., increase in drag) and undesirable aeroelastic effects. [1-4]

The flow physics of the interactions of shock waves with surface boundary layers has been the subject of extensive investigations since the 1940s. The early investigations[5-8] established details of the complex nature of these interactions with laminar and turbulent boundary layers at transonic speeds. The interaction of an incident oblique or normal shock wave (which can be caused by an irregularity in wall shape, such as a corner or a step) results in concomitant alteration of both the velocity distribution within the boundary layer and in the wave pattern in the external flow and is typically accompanied by a local flow separation downstream of the shock (e.g., Adamson and Messiter[9]). In particular, the interactions of shock waves with turbulence can lead to substantial unsteadiness and deformation of the shock while the characteristic velocity, timescales and length scales of turbulence change considerably.[10]

The influence of shock waves on transonic flow over airfoils was of much interest due to unfavorable flight characteristics of traditional subsonic airfoils,[11] most notably efforts to better understand the 'pitch-up phenomenon', and gain a better understanding of shock induced drag. The adverse effects of shock boundary layer interactions have prompted much interest in their mitigation using flow control approaches (e.g., Dolling[12]) with varying degrees of effectiveness. Conventional flow control approaches applied to a variety of situations were reviewed in extensive detail by Pearcey[1], including, relevant to the current study, a section which reviews boundary layer control applied to a half-airfoil or a 'bump'. An updated overview of shock control strategies is provided by Delery[2], including passive (use of vortex generators and local changes in surface contour) and active (suction and blowing or bleed at the surface, surface cooling) control. The author noted that some of these techniques can be used to either modify the boundary layer upstream of the shock to increase its "resistance" to separation, or can be applied underneath or immediately downstream of the shock. A comprehensive review of early work on the suction and blowing for controlling shock boundary layer interactions was later presented by Viswanath[3]. Several authors (e.g., Lin[13]) described suppression of shock boundary layer separation by the introduction of streamwise vorticity upstream of the shock using low-profile, sub-boundary layer (ramp and vane) configurations of vortex generators (VGs). Ashill et al.[14] reported simultaneous increase in lift and decrease in drag by placing the VGs upstream of a normal shock on an airfoil in transonic flow. Vortex generators placed upstream from a compression corner were successful in reducing fluctuations associated with shockwave unsteadiness[15]. Other passive methods applied to shock boundary layer interactions, shown to reduce drag, are porous surfaces and slots. These, along with a number of other flow control techniques designed to reduce wave drag, were explored in the EuroShock II project, the results of which were compiled and edited by Stanewsky et al.[16]. Holden and Babinsky[17] showed that both ramp and vane VGs significantly suppressed separation induced by a normal shock within a test section duct at $M = 1.5$. However, the authors noted that the VGs which were placed directly underneath the shock also increased the wave drag. In a recent numerical study, Lee et al.[18] demonstrated suppression of separation induced by a terminating normal shock within a diffuser ($M = 1.3$). Passive flow control, in the form of an upstream fence, was shown to have an effect on the aero-optical environment of shock induced separated flow.[19]

Active flow control approaches based on continuous suction and blowing have also been applied for mitigation of shock-induced separation by modification of the boundary layer upstream of the shock. Wallis and Stuart [20] demonstrated the use of vortex generating jets on an airfoil-shaped surface to reattach separated flow, the streamwise vorticity generated is shown to have favorable effects both upstream and downstream of the transonic shock. It is notable that their efforts resulted in translation of the shock wave position over a range of pressure ratios. Englar [21] investigated several different blowing strategies applied to elliptic airfoils at transonic speeds showing, using lift and drag comparison, that tangential blowing over an elliptical surface provided the best performance. Krogmann et al.[22] demonstrated that high-aspect ratio suction upstream of a normal shock over an airfoil in transonic flow ($M = 0.78$) at off-design conditions led to reduction in the boundary layer thickness and improved the overall aerodynamic performance by delaying the rapid growth of the separation bubble and stabilizing the shock. These authors noted that even the inactive suction slots (and underlying cavity) had significant beneficial effects in terms of reduction in separation and buffeting ostensibly due to coupled cavity feedback. Souverein and Debieve[23] used a spanwise array of sub-mm, continuous jets for generation of streamwise vorticity for suppression of boundary layer separation induced by an oblique-shock on a test surface at $M = 2.3$, and noted that the reduction in the characteristic scale of the separation bubble was accompanied by an increase in the frequency of the energetic spectral components of the reflected shock.

More recently, the effectiveness of novel flow control technologies for mitigation of adverse shock boundary layer interactions has been investigated. Kalra et al.[24,25] conducted numerical and experimental studies of magneto-gasdynamic plasma actuators where directional (streamwise-oriented) plasma actuation is effected by a magnetic field. They reported reduction in the separated region with best results when the plasma actuator was positioned at the shock impingement zone. Another approach for controlling an oblique shock was presented by Narayanaswamy et al.,[26] who used a thermally driven synthetic jet (using electric discharge) to lock the shock-wave oscillations to the jet pulsating frequency (about 2 kHz) indicating potential for shock stabilization at higher actuation frequencies. For a comprehensive discussion of shock wave boundary layer interactions and their control see a review by Babinsky and Harvey.[27] Vukasinovic et al.[28] recently explored two active flow control approaches, namely 'direct' and 'indirect', for the transonic shock and its coupled flow separation control, with an emphasis on the large scale unsteadiness of the separated flow.

The primary goal of the present investigation is to assess the effectiveness of *indirect*, active flow control of the static and dynamics characteristics of a transonic shock. The flow control approach focuses on the shock-induced

flow separation (downstream of the shock), rather than on the shock itself. The global flow features in the absence and presence of actuation are characterized using a rounded ramp surface geometry, which induces a transonic shock and allows for shock motion in the absence of surface discontinuities.

II.   Experimental Setup and Diagnostics

The present experiments were performed in a small, open-return pull-down high-speed subsonic wind tunnel (test sections speeds of up to $M \approx 0.74$), driven by a 150 HP blower. The schematic of the test section is shown in Figure 1. The modular test section measures $12.7 \times 12.7 \times 61$ cm, and the temperature of the return air is controlled using a chiller coupled with an ultra-low pressure drop heat exchanger. Two static pressure ports and a temperature probe are integrated into the tunnel wall for calibration and monitoring purposes. The first pressure port p_i and the temperature sensor are positioned immediately downstream from the tunnel inlet contraction, upstream from the test section. The second pressure port p_e is placed just upstream from the test section exit plane (Figure 1a). The test section having a nominal square cross section is calibrated using a Pitot probe at its center. The calibration is done relative to the pressure drop across the inlet contraction ($\Delta p = p_{ig}$), and the resulting calibration curve is shown in Figure 1b. The test section Mach number could be raised up to about $M = 0.74$ in the absence of any test model.

A detailed layout of the 2-D test geometry, along with integrated diagnostic components, is shown in Figure 2. The upper, nominally flat, wall of the test section is fitted with a gradual ramp that terminates as an aft surface of the
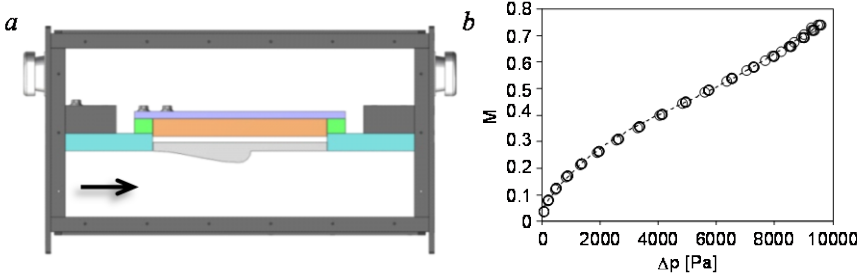

radius $4H$ ($H = 20$ mm) that extends up to $L = 2.6H$ past the apex. This aft geometry is selected as a generic convex surface that induces a localized shock formation in transonic flow conditions, and is adequate for studying the flow dynamics related to separated flows induced by the boundary layer separation in both adverse pressure gradient and the shock-boundary layer

Figure 1. *Schematics of the Georgia Tech test section (a) and the test section calibration (b).*

interaction. Although assessing its full dependence is outside of the scope of the present study, it is argued that the resulting shock dynamics would be dependent on the actual surface curvature due to the altered pressure gradients.

The model geometry is composed of three sections, such that the first one consists of part of the ramp, the second is the main interchangeable section that can have the control devices built into it, and the third one represents the downstream wall. All of the model sections integrate into the upper wall of the tunnel test section. Each central interchangeable section has fifteen static pressure ports distributed along the model centerline (p_1–p_{15}). Besides the static pressure measurements, two dynamic pressure sensors are flush-mounted upstream p_u and downstream p_d from the model geometry at x/H = -2.95 and 3.13, respectively. The baseline and controlled flow fields are characterized by planar high-speed PIV measurements (field of view shown in Figure 2), where each set of data is recorded at 3,133 fps. The mean flow fields and the statistics derived from the instantaneous velocity fields are based on ensembles of 2,700 image pairs. For convenience, all PIV flow fields are shown in an inverted view. Lastly, the flow fields were characterized by schlieren visualization, where its field of view is centered about the aft section of the ramp, as schematically shown in Figure 2. The single-pass schlieren setup incorporated a continuous light source passing through the 800 μm pinhole. The schlieren images were captured by a digital camera at 15 fps and at the exposure time of 5 μs.
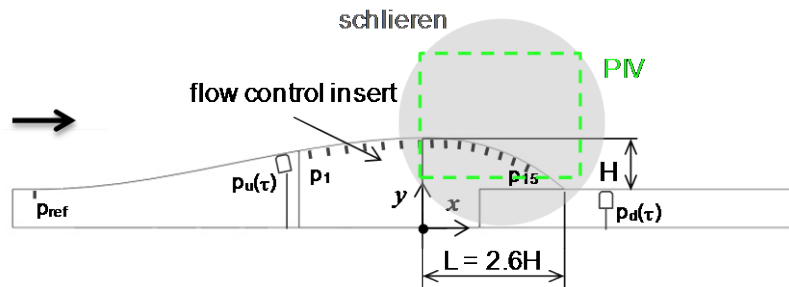

Figure 2. *Schematics of a 2-D model.*

The nominal flow over the test geometry was first characterized by the upstream (p_i) and downstream (p_e) pressure measurements over a full range of the tunnel speeds. The resulting reference pressures over measurement sets of d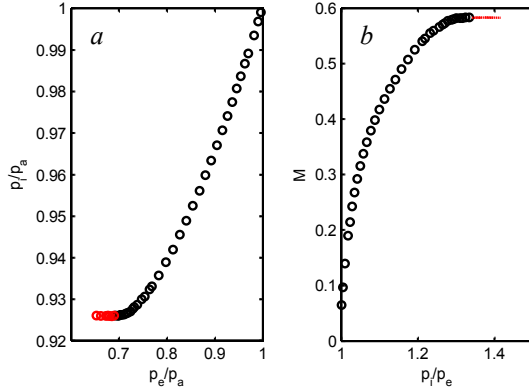ifferent speed increments are shown in Figure 3. As the tunnel speed increases, both p_i and p_e decrease accordingly, up to the point when the upstream pressure begins to level, which indicates the test section choking point. As the mass flow rate is invariant in the choked flow regime, further increase in the blower suction results only in further lowering of the back pressure, illustrated by continuing decrease in p_e for invariant p_i, as marked in red in Figure 3a. After the test section flow becomes choked, the upstream pressure becomes invariant and the tunnel calibration (Figure 1b) cannot be used to characterize the oncoming flow state. Consequently, calibrated upstream Mach numbers can be used as reference parameters in the pre-choked flows and downstream pressures p_e can be used for reference in the choked flows. Alternatively, the pressure ratio p_i/p_e can be used to characterize the upstream flow state throughout all of the flow regimes. Figure 3b shows a relationship between the test section Mach number and the pressure ratio p_i/p_e up to the choking condition, which is shown by the dashed line.

Figure 3. *Characterization of the tunnel flow over the test ramp geometry: pressure p_i downstream from the inlet contraction with p_e at the test section end (a) and tunnel Mach number with the p_i/p_e (b).*

The planar high-speed PIV measurements are used to extract the instantaneous shock wave position. First, it should be noted that due to the high laser intensity necessary for the high-speed PIV, intense surface reflections masked the flow 'strip' immediately near the surface in spite of the surface anti-reflective treatments. Therefore, all the measured flow fields exclude the near-wall region, which is masked hereafter. Also, the full PIV fields of view spread across the edge of the optical window which very edge is captured in the upper right corner of the flow field, and that corner is also masked in the presented flow fields. To extract the shock positions, horizontal component of velocity field is first plotted at each discretized elevation y/H, such as the one marked by the dashed line in Figure 4a. The corresponding instantaneous velocity traces are shown in Figure 4b in grey with the average velocity overlaid in red for clarity. All velocity fields are shown relative to the reference velocity U_{ref} of the oncoming flow at the choking condition. When a shock wave is present in the flow field, the velocity 'jump' across the shock is quite distinguishable. The shock wave position for each particular elevation y/H and particular instant in time is defined by finding the minimum slope within the velocity 'jump' region. Shock wave positions associated with the velocity traces in Figure 4b are shown in the form of a histogram in Figure 4c, where $n_i = N_i/\sum N_i$ for each spatial bin $\Delta x/H$. This process is repeated for all flow fields for all feasible y/H elevations and all of the positions are displayed on top of a time-averaged raster plot in Figure 4a, which also illustrates a full domain of the shock motion.

Instead of passive control devices typically used in the control of transonic shock,[27] the present work utilizes their fluidic counterpart, fluidic oscillating jets. These jets sweep in the spanwise direction, and hence in the plane normal to the PIV measurement plane in a manner that is illustrated schematically in Figure 5a. These fluidic oscillating jets combine the benefits of unsteady flow control due to their oscillating nature and a net added mass
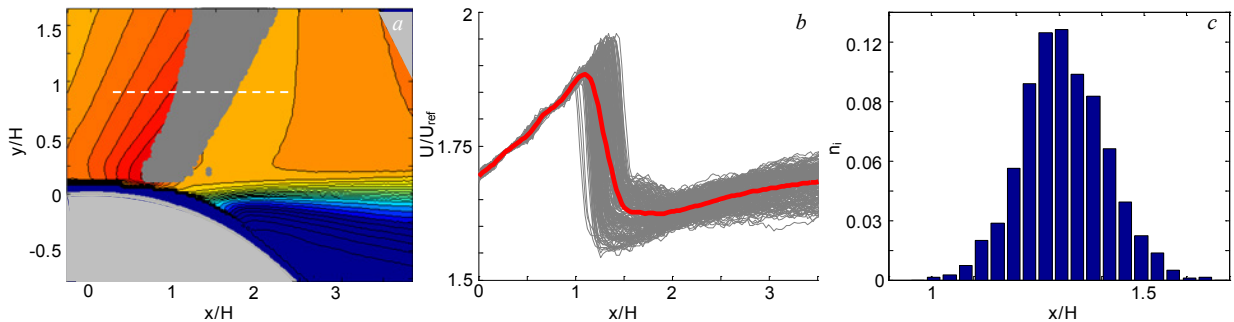
Figure 4. *Overlapped discretized shock positions for the baseline flow at $p_i/p_e = 1.36$ (a), the corresponding streamwise velocity profiles across the shock at the marked elevation (b), and histogram of the shock streamwise positions x/H (c).*

and momentum to the flow, which assist in the Coanda effect over the curved surface. Seventeen such fluidic oscillating jets are equidistantly distributed across the model span. Each jet orifice is 1.5×1.5 mm and neighboring jets are spaced 7.5 mm apart. The resulting flow effects are tested for four jets total mass flow rate coefficients $C_q \times 10^3 = 0.6$, 1.7, 2.6, and 4, for both the pre-choked and the choked flow regimes (C_q is defined as the ratio between the total mass flow rate through the jets and the mass flow rate through the test section). It should be noted that the corresponding momentum coefficient C_μ is defined as $C_\mu = C_q U_j/U_o$, however the jet velocity U_j is not measured in the present study. Nonetheless, even if the jet velocity were up to sonic, given the Mach number in excess of $M = 0.5$, maximum C_μ would be less than twice the maximum C_q utilized in the presented study. The jets' oscillating frequency depends on the fluidic oscillator flow rate and for a typical flow rates utilized in the current test, the frequency is about 10 kHz. To illustrate the oscillating nature of the control jets, three schlieren images captured during the jet oscillation are shown in Figure 5b. Three arbitrary phases during the jet oscillation illustrate the jet motion from approximately left-most to the right-most positions, while passing through the symmetry axis during half of the oscillating cycle.
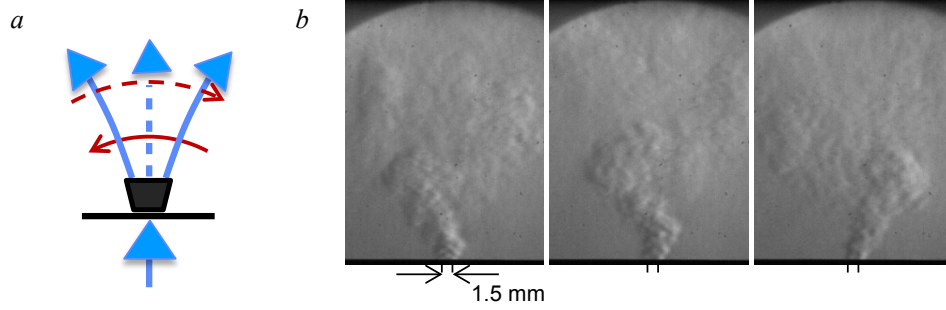

Figure 5. *Schematics of the fluidic oscillating jet operation (a) and its schlieren visualization (b).*

III.   The Baseline Flow

As the pressure ratio across the test section is increased, the flow features over the ramp become dominated by shock wave induced separation, which is of primary interest for the current study. Before this transition, the flow over the ramp results in subsonic separation induced by adverse pressure gradient. To illustrate the global features of both subsonic and shock-induced separation, two mean flow fields over the ramp are shown in Figure 6 in terms of the raster plots of the streamwise velocity component U. Two flow states are selected such that one represents the flow at the pressure ratio p_i/p_e below (Figure 6a) and above (Figure 6b) the critical pressure ratio for the shock formation. Prior to the shock formation (Figure 6a), the flow accelerates up to the ramp apex and then decelerates up to the point that the growing boundary layer cannot withstand the adverse pressure gradient. As the flow separates, the ensuing shear layer grows moderately, as seen in the downward slant of the upper bound of the separated region. Contrary to this scenario, when the critical Mach number is reached at the apex the flow continues to accelerate and terminates in a shock (Figure 6b), the underlying shock-boundary layer interaction induces discontinuous boundary layer thickening which, combined with the adverse pressure gradient, induces its 'premature' separation off the surface. Besides the related increase in the separated flow domain downstream form
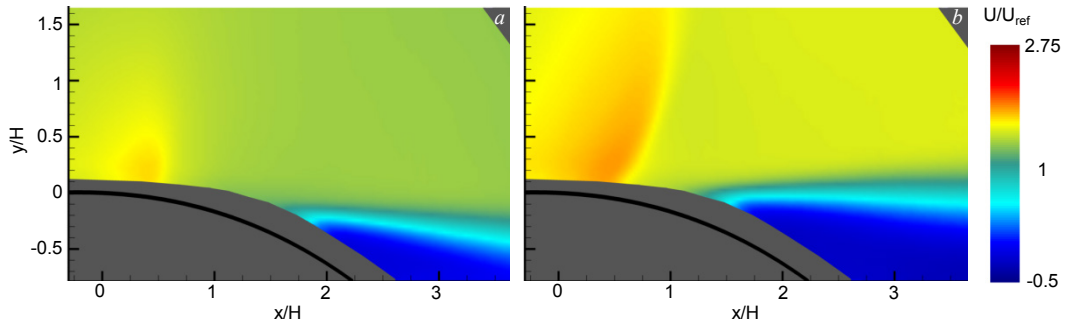

Figure 6. *Raster plot of the mean streamwise velocity component for the baseline flow subsonic (a, $p_i/p_e = 1.25$) and shock-induced (b, $p_i/p_e = 1.32$) separation.*

the incipient separation under the transonic shock, an additional difference relative to the subsonic separation is that the shear layer growth is aggressive, thus opening the upper boundary of the separated region and thereby enlarging the separated flow domain even more compared to the subsonic flow over the ramp.

Baseline flow characterization is done by the static pressure measurements along the ramp centerline. A dedicated computer-controlled *Scanivalve* pressure scanner was used for the pressure measurements. Two sets of pressure ports are distributed upstream and downstream from the model apex, having a gap within a region that is populated by the flow control elements. The pressure ports' coordinates are defined relative to the apex of the contraction ($x/H = 0$), and hence the pressure ports' negative coordinates indicate their upstream position relative to apex. All the static pressures are shown in terms of the compressible pressure coefficient C_p, where the reference pressure p_{ref} (Figure 2) and the oncoming Mach number M are used as the reference parameters.
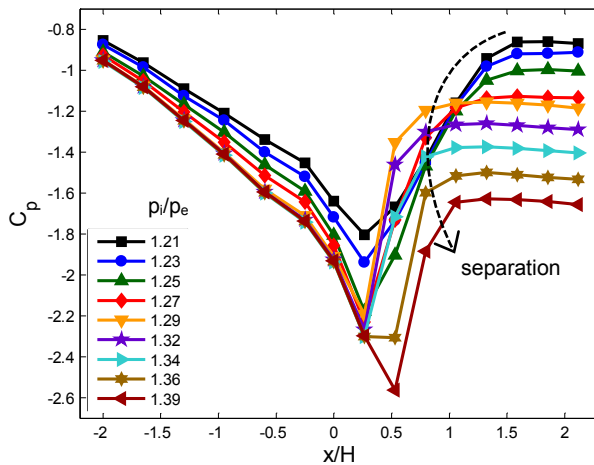

Figure 7. Surface static pressure profiles with increasing p_i/p_e.

Figure 7 shows the measured surface pressure profiles for the varying tunnel speeds without the flow control elements embedded into the surface. The array of pressure profiles upstream from the apex indicate a typical evolution over a mildly converging surface, while downstream from the apex the flow becomes fully separated by $x/H = 1.5$, regardless of the Mach number. The second notable feature is that the pressure profiles also indicate that the flow becomes choked at higher Mach numbers, as all of the upstream pressure profiles virtually collapse onto the same curve for the pressure rations $p_i/p_e > 1.29$. In accord with the flow field illustration in Figure 6, the subsonic pressure profiles ($p_i/p_e < 1.27$) indicate that the flow remains attached nearly up to $x/H = 1.5$. The initial formation of the shock ($p_i/p_e = 1.27$) seems to shift the flow separation ups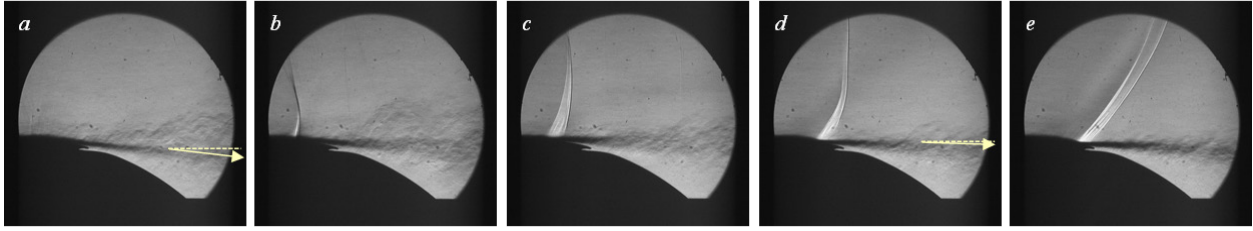tream but not to lock it to the shock position, while the next flow condition ($p_i/p_e = 1.29$) clearly indicates the shock-induced separation, as well as all the following conditions with the increasing pressure ratio. In addition, it is interesting to note that the separation point moves downstream with an increase in the pressure ratio above 1.29, so that the separation point moves upstream at the transition from subsonic to transonic flow regime, and then continuously shifts downstream with an increase in the pressure ratio, as marked by the dashed line in Figure 7.

Additional global characteristics of the baseline flow are illustrated in a series of schlieren images shown in Figure 8 over the ramp model with the surface-integrated flow control elements. Prior to formation of the normal shock past the apex of the ramp, the only sharp density gradient exhibited in the flow field is generated by the incipient shear layer of the separating flow in the adverse pressure gradient, as seen in Figure 8a. The image in Figure 8a is taken at $M = 0.54$, prior the formation of a visible shock. Significant pressure/density variations upstream from the flow separation are observed as the upstream Mach number is increased, the first highly unsteady normal shock is observed at about $M = 0.57$ (Figure 8b). This local density gradient is initially weak and unstable, but, with a steady increase in the upstream Mach number (Figures 8c–d), it gradually gains in strength (marked by an increase in density gradient), localizes downstream from the ramp apex, and extends further outward, towards the opposite wall. Nonetheless, the shock appears to be highly unsteady and oscillates in all instances, although these oscillations do not appear to be synchronous. Initial formation of the shock appears to shift the flow separation upstream (compare Figures 8c and a). Furthermore, a notable oscillation of the incipient shear layer is observed as well. As the upstream Mach number is further increased, the shock extends to the opposite test section wall, rendering the tunnel flow choked, which state is shown in Figure 8e. It is notable that the shock also begins to tilt slightly forward, which becomes increasingly prominent with further decrease of the back pressure. As already stated, the flow mass rate does not change in the choked regime, and further increase in the pressure ratio only lowers the tunnel pressure downstream from the shock. The shock location also shifts somewhat downstream, as already seen in the separation point shift in Figure 7. The concomitant shift in the shock position and separation point also indicates the shock-induced nature of the flow separation.

Figure 8. *Schlieren visualization of the baseline flow separation M = 0.542 (a), 0.572 (b), 0.583 (c), 0.586 (d), and the choked flow (e).*

Due to the subsonic flow regime downstream from the transonic shock, any pressure disturbances can propagate upstream and induce temporal imbalance of the pressure field across the shock. It is also reasonable to expect that the upstream pressure fluctuations/disturbances carried through the oncoming boundary layer would be secondary to stronger sources of disturbances downstream from the shock, which can originate in the shear layer formation and/or global unsteadiness of the flow reattachment downstream from the shock. Clearly, besides the flow-related sources, it is also possible that some facility-related disturbances impose pressure imbalances across the shock. In a response to any imbalances, the shock position must change to match the change in boundary conditions. As the flow is highly two-dimensional the physical movement of the shockwave is not uniform at all points on the shockwave. Depending on the complex interplay between the initial pressure imbalance and the shock's altered position and shape, such a response to initial pressure imbalance can lead to secondary pressure imbalance, which can in turn lead to the new shock adjustment of position/shape. These dynamics can finally lead to shock oscillations, which are further complicated by the shock's coupling to the flow separation as the shock oscillations may momentarily decouple the shock position and the flow incipient separation.
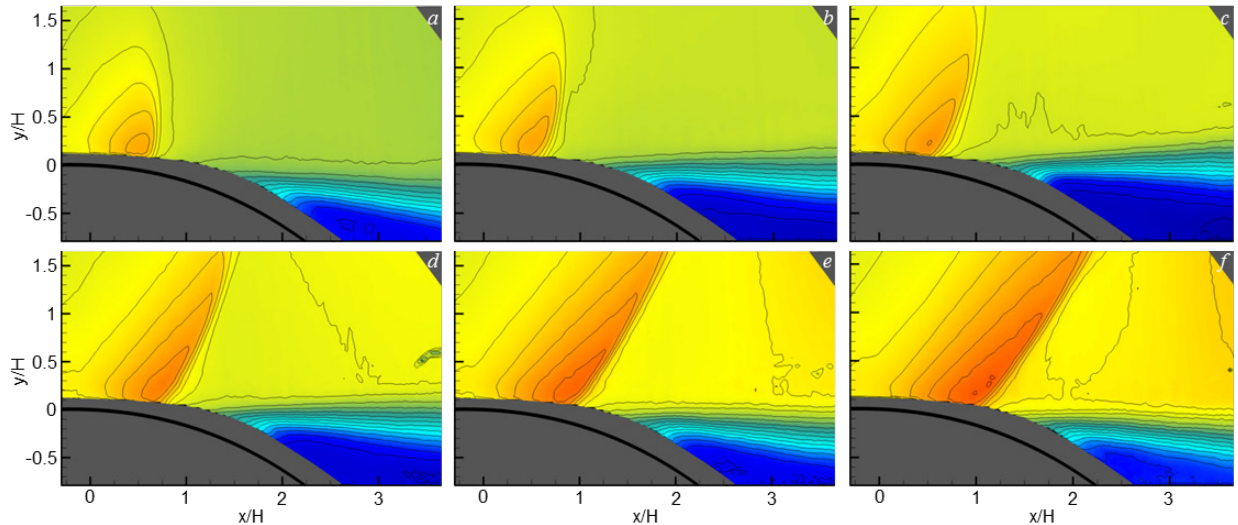

Figure 9. *Raster plots of the conditionally-averaged mean streamwise velocity component for the most-probable shock location at p_i/p_e = 1.27 (a), 1.29 (b), 1.32 (c), 1.34 (d), 1.36 (e), and 1.39 (f).*

As it is illustrated in Figure 4 and discussed above, the shock wave position is unsteady, and as a consequence an ensemble average of the captured PIV flow field for a given flow condition is not fully representative of the shock wave position, strength and structure. In order to elucidate shock-related features of the flow fields, the full ensemble of the PIV data sets is further conditionally averaged over spatial bins $\Delta x/H$, as described in discussion of Figure 4. After the most probable shock position is deducted from the histogram (see Figure 4c) at the peak occurrence, all the flow fields that contain the shock within the most probable spatial bin are subsequently averaged. The resulting conditionally-averaged flow fields over different pressure ratios p_i/p_e are shown in Figure 9 in terms of the contour plots of the streamwise velocity component. It should be also noted that the split averaging with respect to the shock either downstream or upstream motion with the bin resulted in indistinguishable flow fields, which could be a consequence of a narrow spatial bin $\Delta x/H$. Comparison between the ensemble- and conditionally-
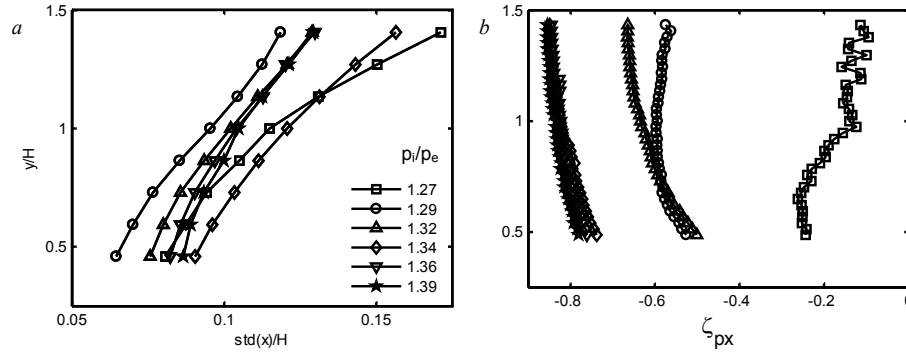
Figure 10. *Standard deviation of the shock position (a) and cross-correlation between the shock position and the pressure p_d (b) with the elevation y for the uncontrolled flows.*

averaged flow fields, such as Figure 6b and Figure 9c, shows that the 'most probable' conditionally-averaged shock position coincides with the averaged shock position, while the former resolves sharper velocity gradients associated with the shock and hence better isolates the shock.

Additional insight into the shock dynamics is sought through a measure of its oscillation about the most probable position and its displacement correlation with the pressure field in the separated flow. Therefore, evolution of the shock dynamics over different uncontrolled flows is illustrated in Figure 10 in terms of the standard deviation of its oscillation (Figure 10a), and the correlation between the downstream pressure signal $p_d(\tau)$ and the instantaneous shock position $x(\tau)$ over the different shock elevations away from the wall (Figure 10b). The one behavior that deviates from all the other trends in both characterizations is a case of the lowest tunnel speed ($p_i/p_e = 1.27$), which is also characterized in the pressure profile (Figure 7) as the case that appears not to directly induce the flow separation at the shock origin, but only to induce premature separation upstream from its subsonic origin. The magnitude of the shock oscillations increases with distance away from the surface for all the baseline flows, with only the shock formed at $p_i/p_e = 1.27$ having a somewhat more pronounced dependence of the oscillation magnitude with height compared to the other cases. The pressure $p_d(\tau)$ and the shock position $x(\tau)$ correlation sign (Figure 10b) clearly indicates that an increase of one induces a decrease of the other, which is aligned with a notion that an increase in the back pressure of the shock would induce a pressure imbalance that triggers the shock upstream motion (having a decrease in x position). Other notable feature of the correlation function is a nearly discontinuous increase in the correlation magnitude with an increase in the pressure ratio. There is a rather weak correlation for the lowest pressure ratio that is shown not to couple to immediate shock-induced flow separation. Once the shock directly induces the flow separation, there is a considerable increase in the pressure-shock position correlation. Finally, once the flow is choked, the correlation level increases even further to levels in excess of -0.8.

IV.   The Controlled Flow

The present active control approach builds on the exploratory work by Vukasinovic et al. (2013), where, in one of the approaches, the transonic shock was manipulated not by its direct control, but rather by control of the separated flow resulting from the shock wave and boundary layer interaction. Such a control approach relies on the coupling between the shock, incipient boundary layer separation and the large-scale unsteadiness of the separated flow. When the flow control is capable of effecting the flow separation by altering its dynamic and static (mean) properties, the corresponding altered pressure field couples to the shock and affects its static and dynamic characteristics. The present objective is to investigate relationship between the active flow control source (fluidic oscillating jets, Section 2) and the shock static and dynamic response.

Figure 11 shows the static pressure profiles for the two flow regimes over the ramp. Both flow regimes exhibit similar features expressed through the surface static pressure field. As the flow accelerates of the ramp, it turns sonic and continues to accelerate past the geometry apex (compare to the subsonic flow acceleration in Figure 7). At the point of shock formation, there is a sharp rise in pressure, followed by the pressure leveling due to the coupled flow separation. There are several important features to be noted with respect to the controlled-flow pressure profiles. First, there is virtually no effect on the global flow upstream from the apex. Second, as C_q increases, there is a clear shift in the separation point of the flow, i.e., the higher flow control rates induce a further delay in the flow separation off the aft surface. Consequently, the separation pressure level increases, too.
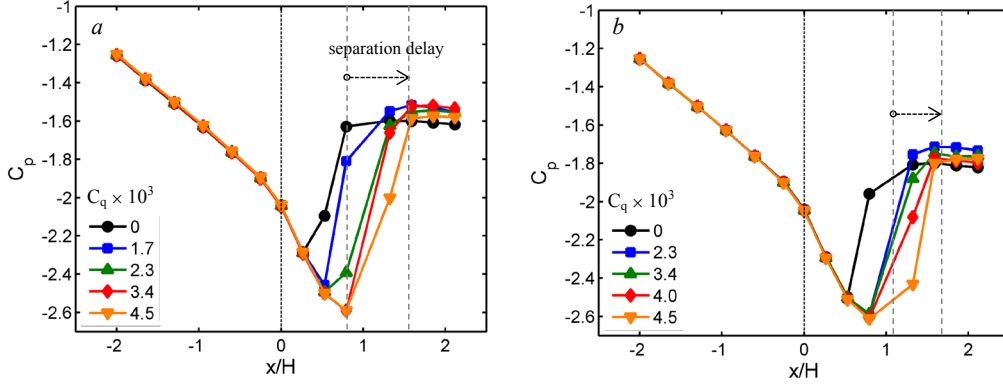
Figure 11. *Static pressure profiles for the baseline flows (●) and the flow controlled by the varying C_q at p_i/p_e = 1.34 (a) and 1.39 (b).*

In conjunction with the static pressure profiles shown in Figure 11, it is informative to assess the global features of the two dynamic pressure sensors, p_u and p_d. Figure 12 shows the two parameters of the time-dependent pressure measured by these two transducers: time-averaged pressure and its standard deviation as a measure of its variance about the mean. The data are shown for all the tested flow regimes. As expected, based on the static pressure profiles upstream from the apex (Figure 11), the active flow control does not alter the mean pressure field at the upstream transducer p_u at any flow control rate. The downstream transducer p_d shows a clear direct dependence on the flow control rate: the mean pressure increases proportionally to the control flow rate at all of the flow regimes, and the proportionality coefficient decreases with an increase in the test section pressure ratio, which is a direct consequence of the fixed flow control rate. Similar to the mean pressure dependence on the flow control rates, the upstream pressure standard deviation is not affected by the active flow control, while the downstream pressure fluctuations increase with the increase in the flow control rates. This increase is attributed both to the unsteadiness that the fluidic oscillating jets introduce into the shear layer and the separated flow and to the suppression of recirculating domain due to the flow separation delay. The results presented in Figures 11 and 12 suggest that, in a static sense, there is a clear relationship between the flow separation delay (shock position) and the downstream pressure p_d, which implies that such a pressure signal might be a good candidate for the closed-loop control sensor.

The corresponding qualitative effect of the flow control on the shock, shear layer, and the separated flow global features can be surmised from the accompanying schlieren images shown in Figure 13, for the two flow regimes. The upper sequence focuses on the flow regime that results in the baseline flow acceleration terminating through the normal shock (Figure 13a). Shlieren visualization indicates that the flow separation originates at the base of the shock, resulting in a nearly-horizontal shear layer. As the control jets are activated at the lowest C_q (Figure 13b), the shock becomes displaced downstream and tilts forward. Although the forming shear layer immediately behind the shock does not exhibit much difference from its baseline counterpart, the remaining shear layer thickens and
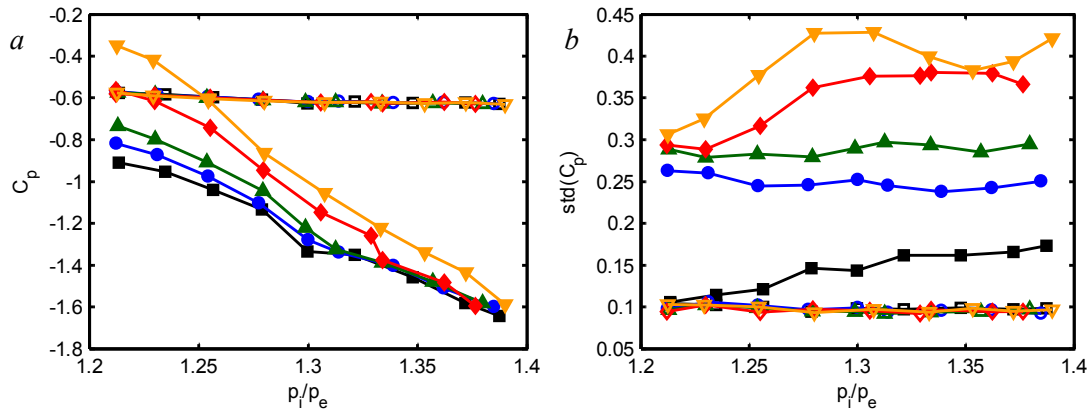

Figure 12. *Time-averaged (a) and standard deviation (b) of the dynamic pressure profiles with the tunnel speed of the upstream (open symbols) and downstream (solid symbols) transducers for $C_q \times 10^3$ = 0 (■), 0.6 (●), 1.7 (▲), 2.8 (♦), and 4 (▼).*
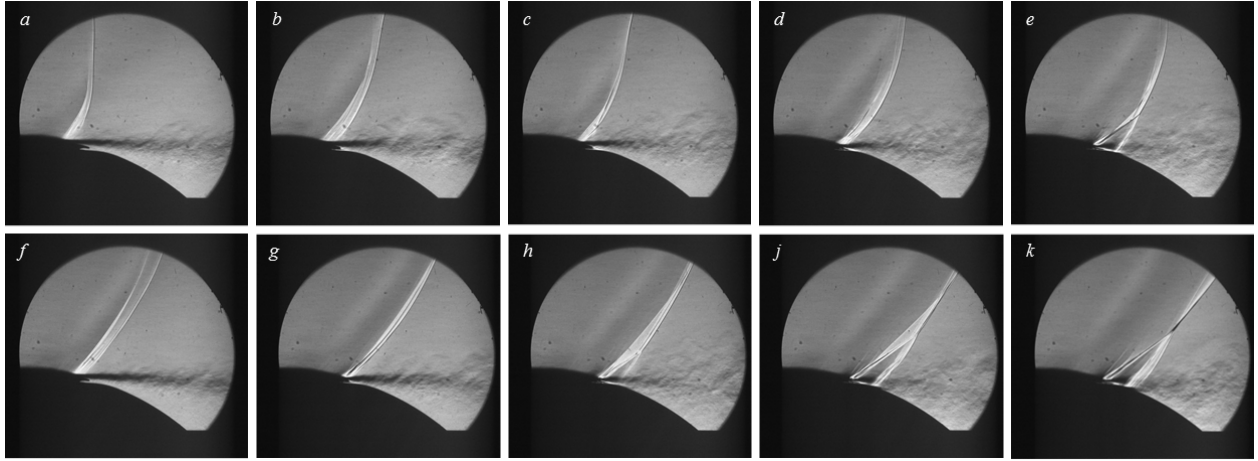
Figure 13. *Schlieren visualization of the uncontrolled flows at pi/pe = 1.34(a) and 1.39 (f), and the corresponding flow control cases (b – e) and (g – k) at $C_q \times 10^3$ = 1.7 (b), 2.3 (c,g), 3.4 (d,h), 4 (j), and 4.5 (e,k).*

somewhat diffuses the sharp density gradients. Further increase in C_q (Figures 13c and d), further displaces the shock and enhances the shear layer spreading and diffusion of sharp density gradients, a clear indication of the increased mixing. Hence, it can be argued that the control effect of the active control jets is twofold: it both delays the flow separation and enhances the shear layer mixing, once the flow becomes separated. The highest flow control rate (Figure 13e) induces a formation of the lambda shock over the surface geometry, which should assist in overall weakening of the shock. At the same time, this state clearly represents the most diffused and spread shear layer having the lowest density gradients. The choked-flow regime under the higher pressure ratio (lower row) depicts a similar evolution of shock-induced separation with the flow control. The baseline state (Figure 13f) has a markedly different shock from the lower pressure ratio flow regime (Figure 13a), as the shock is clearly tilted in the downstream direction, and its origin is displaced slightly downstream. Nonetheless, the overall features of both shear layers are quite similar. Once the flow control is applied, analogous effects to those already discussed are observed, and the flow control results in simultaneous separation delay and the enhanced shear layer mixing. The lambda shock also becomes formed at the two highest flow control rates.

The mean flow fields for the p_i/p_e = 1.36 flow regime are shown in Figure 14 contour plots in terms of the mean streamwise velocity for the baseline, and the flows controlled by C_q = 1.7, 2.8, and 4 × 10^{-3} fluidic oscillating jets. Although the ensemble-averaged flow fields inevitably diffuse and relax the measured shock wave due to its
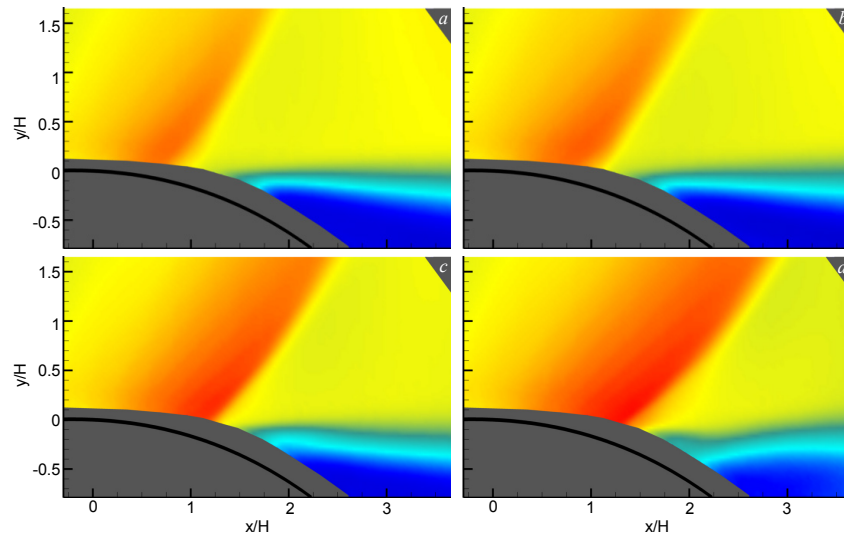

Figure 14. *Raster plot of the mean streamwise velocity component for the uncontrolled (p_i/p_e = 1.36) flow (a) and the controlled flows at $C_q \times 10^3$ = 1.7 (b), 2.8 (c), and 4 (d).*

unsteady nature, it is still informative to assess the averaged shock and separation location in each of the flow control cases, as well as their impact on the shear layer. Besides, comparison between the mean and conditionally-averaged flow fields in Figure 6b and 9c pointed to similar gross flow features with the matching shock positions and shapes. Furthermore, contrary to the schlieren visualization that integrates across the whole optical path, PIV-generated flow fields are averaged only across a single vertical plane, or along one 'slice' of the integrated schlieren visualization. Nonetheless, the overall flow features remain similar. As it was already shown in the schlieren visualization, the baseline flow shock-induced separation (Figure 14a) results in a nearly-horizontal shear layer that opens up into significant domain of the separated flow downstream from the ramp. As the flow control is applied, the separation point shifts downstream with C_q, and the separated domain becomes suppressed. It is interesting that the appearance of the lambda shock at the highest flow control rate appears to displace the shear layer away from the surface, as it appears to 'buckle' at the highest flow control rate (Figure 14d).

To quantify the shock static displacement with the flow control, all the averaged shock positions are extracted from ensembles of the PIV flow fields for all the baseline flow regimes and shown in Figure 15. Figure 15a shows the shock displacement with C_q for $p_i/p_e = 1.36$. Clearly, the shock position shifts downstream with an increase in C_q, and the shock exhibits weakly increasing tilt. The shock position x' at $y/H = 1$ is selected as a reference measure of the shock downstream displacement, as schematically shown in Figure 15a. After extracting all the reference shock positions for all the pressure ratios for the uncontrolled flows, they are plotted in Figure 15b, where it is seen that the shock traverses from about $x/H = 0.7$ to just above $x/H = 1.4$ over that span of the pressure ratios p_i/p_e. Therefore, the shock displacement is directly proportional with the pressure ratio of the uncontrolled flows. Figure 15b also shows all the corresponding shock positions for the controlled flows. There are several features of the controlled shock displacement that should be noted. First, there is a nearly twofold shock displacement from the apex over the full control span regardless of the test section pressure ratio. Second, besides the two lowest p_i/p_e flow regimes, the presented data indicate that the active flow control somewhat reduces the pressure losses across the test section for all the flow control cases but the highest ones. The initial reduction in the controlled p_i/p_e is attributed to the suppression of the separated domain via separation delay and increased shear layer mixing, while the leveling and reversal of the effect at the highest C_q is attributed to the opposing effects of the separation delay and the 'buckling' of the shear layer that was observed in both the schlieren visualization and the PIV characterization of the flow field.
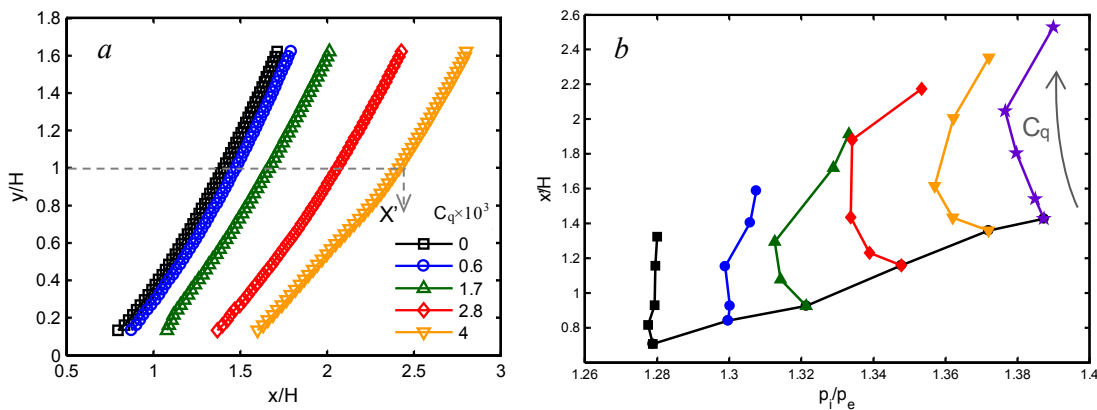

Figure 15. *Time-averaged shock profile at $p_i/p_e = 1.36$ (a) and the shock position x'/H with p_i/p_e for the baseline flow (open symbols) and controlled flows (solid symbols) at $C_q \times 10^3 = 0.6, 1.7, 2.8,$ and 4.*

As already discussed in conjunction with Figure 4, besides the shock mean position, further statistics are derived from the instantaneous velocity fields, including the histograms of the time-dependent shock positions. The histograms point to the most probable shock positions, and the bin with the most probable shock position was further utilized for conditional averaging of the flow field only over realizations in which the shock appeared within that 'most probable' spatial bin. Figure 16 illustrates the same flow regimes which mean flow fields are shown in Figure 14. It is interesting to note that the corresponding flow fields in both the mean and conditionally-averaged fields are quite similar, the only markedly difference being that the conditionally-averaged ones depict less-diffused shocks as they are averaged only over the shock realizations within the most probable bin. As it may be expected, the averaged flow fields in Figure 14 adequately capture the mean shock locations, which coincide with the
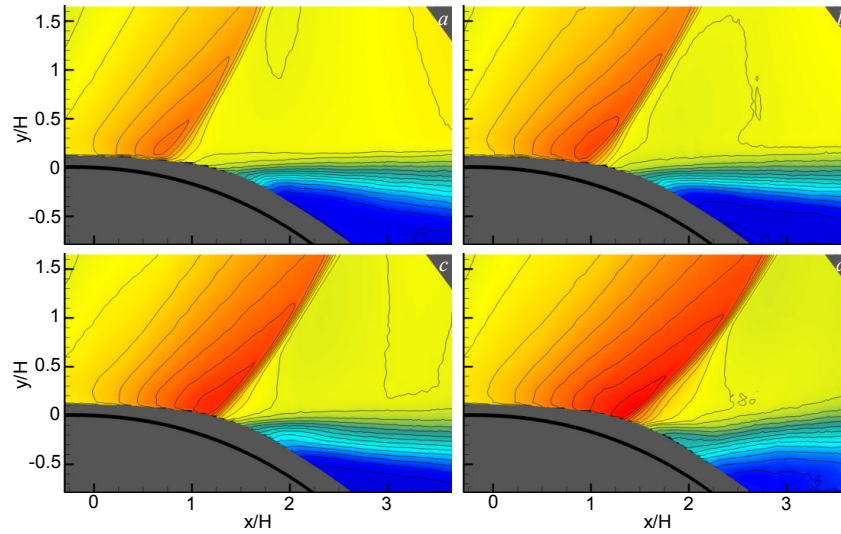
Figure 16. *Raster plots of the conditionally-averaged mean streamwise velocity component for the most-probable shock location for the uncontrolled flow at $p_i/p_e = 1.36$ (a) and the controlled flows at $C_q \times 10^3 = 1.7$ (b), 2.8 (c), and 4 (d).*

corresponding 'most probable' locations of Figure 16. Furthermore, it is interesting to note that even the mean features of the shear layer in Figure 14 resemble the shear layer feature over the most probable realizations of the shock position, which further emphasizes the relevance of the time-averaged global flow features in spite of inevitable distortions of the shock strength and its streamwise extent.

Besides the static effect of the flow control on the shock position, some insight into the shock dynamics with and without the flow control is gained by analysis of the shock oscillations about its mean position. Figures 17a and c shows the vertical profiles of standard deviation of the shock oscillations about its mean position for the
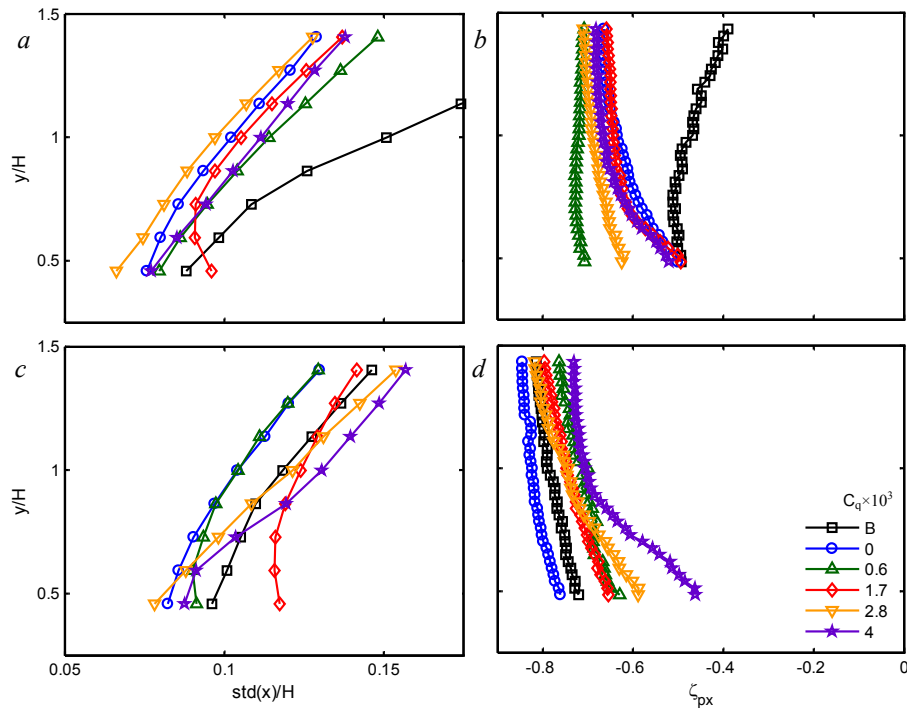

Figure 17. *Standard deviation of the shock position (a, c) and cross-correlation between the shock position and the pressure p_d (b, d) with the elevation y for baseline flow 'B' and the flows controlled at different C_q for $p_i/p_e = 1.32$ (a, b) and 1.36 (c, d).*

uncontrolled flow at p_i/p_e = 1.32 and 1.36, respectively, and under the active flow control at varying C_q. In addition, the corresponding shock oscillations are characterized in the absence of the flow control elements, i.e., over a smooth surface. Regardless of the flow regime, the results indicate that just a presence of the (inactive) flow control elements embedded into the surface significantly suppress the shock oscillations. However, there appears to be a difference with respect to the shock oscillation in the pre-choked flow regime and after the flow is choked, when the active flow control is applied. While the controlled flow generally experiences suppressed levels of the shock oscillations under any C_q in the pre-choked regime (Figure 17a), there appears to be a tendency of the controlled flow to increase the level of the oscillations near the surface at lower C_q and decrease away from the surface, while the trend appears to be reversed at the highest C_q, once the flow becomes choked (Figure 17c). Interestingly, the cross-correlations between the downstream pressure signal $p_d(\tau)$ and the instantaneous shock position $x(\tau)$ also shows different trends for the pre-choked and choked flow regimes, as seen in Figures 17b and d, respectively. The baseline flow under the pre-choked regime shows the least level of correlation (Figure 17b), which remains virtually unchanged near the surface for both the inactive flow control elements, and active at the two lowest C_q. However, the correlation significantly increases with increasing distance from the surface. As C_q is further increased, there is the corresponding increase in correlation near the surface as well, which results in a more uniform correlation between the pressure fluctuations and the shock oscillation across its height. There is a high level of correlation between the shock oscillations and pressure fluctuations even in the baseline chocked flow (Figure 17d), which becomes slightly more pronounced with the flow control elements embedded into the surface and inactive. Contrary to the pre-choked flow regime, once the control jets are activated, the correlation decreases with C_q, particularly closer to the surface.

Given the proportional relationship between the downstream mean pressure p_d and the control jets flow rate coefficient (Figure 12) and similar relationship between the mean shock displacement and the control jets flow rate coefficient (Figure 16), it is expected that the instantaneous pressure readings of the pressure transducer $p_d(\tau)$ would be well correlated with the instantaneous shock position $x(\tau)$. The high levels of correlations were verified in Figures 10 and 17, indicating that the increase in one parameter induces a decrease in the other. Further illustration of the back-pressure shock wave dynamics is shown in Figures 18a and b, where the time traces of the pressure signal and instantaneous shock positions, extracted from the PIV measurements, are plotted at p_i/p_e = 1.36, respectively. There is a clear correlation between the two time traces, which are emphasized by the connecting dashed lines at several large excursions. Furthermore, each positive excursion in the pressure is associated with negative excursion in the shock displacement, and vice versa. To quantify the corresponding flow fields realized at these particular instances, three instantaneous velocity fields are shown at instances that correspond to the large excursions in pressure from the high level at *A* to the low level at *C*, passing through the average level at *B*, as marked in Figure 18b. The corresponding contour plots of the streamwise velocity component are shown in Figures
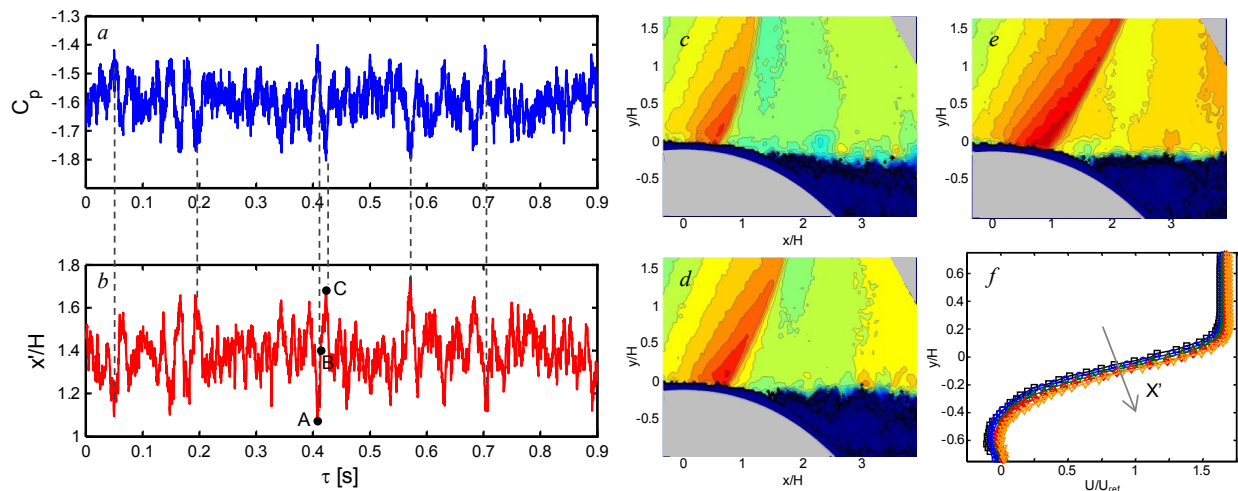

Figure 18 *Time-traces of the downstream dynamic C_p (a) and the corresponding shock positions x'/H (b) for the uncontrolled flow at p_i/p_e = 1.36. Instantaneous flow fields corresponding to times A, B, and C, are shown in (c), (d), and (e), respectively. Shear layer profiles at x/H = 2.5 are shown (f) for conditionally-sampled velocity fields with respect to the shock position.*

18c–e, respectively. It is obvious from the captured flow fields that the shock not only moves downstream with a decrease in downstream pressure from *A* to *C*, but it also changes its shape by continuously increasing its downstream tilt with the downstream displacement. Analogously, it decreases its tilt with the upstream motion (not shown). Although instantaneous flow fields are not necessarily sufficient for determination of the flow separation point with the captured shock displacement, the shown velocity fields suggest that the flow separation point dynamically shifts along with the shock displacement. Further evidence of the synchronous displacement of the shock and the flow separation is seen in the shear layer velocity profiles that are conditionally averaged for the same shock binned spatial position (see Figure 4). The resulting conditionally-averaged shear layer profiles as shown in Figure 18f for the downstream location $x/H = 2.5$. These profiles indicate directly proportional downstream shift in the shear layer profile with the corresponding shock position x', which is another evidence of the flow separation shift with x'.

V.   Conclusions

The present experimental investigation focuses on *indirect* control of a transonic shock by controlling the separated flow domain that is induced downstream of the shock as a result of its interaction with the upstream boundary layer. The flow is controlled by using fluidic actuation across the flow span upstream of separation using an array of fluidic oscillators having characteristic frequencies on the order of 10 kHz.   The transonic shock forms over the curved 2-Dsurface aft of a surface ramp. As the tunnel Mach number increases, the local shock intensifies and ultimately spans the full test section height when tunnel flow becomes choked.

The characteristics of both the baseline and controlled flows are assessed using several diagnostic tools . Some structural features of the shock and of the separated flows are extracted from high-speed schlieren visualization where the field of view is centered about the aft section of the ramp. Both static and dynamic pressure measurements are utilized for measurements of the changes in surface pressure distributions upstream and downstream from the shock. Special emphasis was placed on correlations between the dynamic pressure fluctuations in the separated flow domain and the unsteady shock dynamics. Finally, a high-speed (3,133 fps) PIV measurements in a cross stream plane provide information about the flow upstream and downstream of the shock and the changes that are associated with the actuation.

Pressure distributions in the baseline flow indicate that two flow regimes can be realized in the test section, namely, pre-choked and choked where the pressure distributions upstream of the shock collapse onto single curve past the critical Mach number. Both schlieren images and PIV measurements exhibit the highly unsteady shock oscillations which include both small-amplitude, broad-band high frequency oscillations superposed on larger, low-frequency swings in position. For a given Mach number, the baseline shock is characterized by its mean spatial position, a spread in the broad-band spatial oscillations, and the correlation of shock oscillations with the dynamic pressure downstream.

The shock is dynamically manipulated using active control of the separated flow on the curved surface using a spanwise array of fluidic oscillating jets. The actuation leads to delay of the flow separation by small-scale actuation of the separating shear layer. In response to the alteration of the flow field downstream of the shock, the shock can be displaced and its oscillation amplitude is reduced. The relationships between the actuation amplitude and the magnitude of shock displacement along with the correlation between the shock displacement and surface dynamic pressure downstream of the flow ramp indicate that this actuation approach can be utilized for closed-loop control of the shock stability. The degree of the correlation between the downstream pressure and the shock position depends on whether the flow in the test section is choked. Flow control leads to an increase in the correlation magnitude in the pre-choked flow regime, and results in a decrease of the high correlation levels of the uncontrolled flow in the choked flow. A direct relationship between the streamwise displacement of the shock and the flow control coefficient is established for a broad range of Mach numbers, yielding approximately up to twofold increase in shock displacement from the apex of the test section wall in the presence of actuation.

Acknowledgment

References

[1] Pearcey, H.H., "Shock-Induced separation and its prevention by design and boundary layer control," Boundary Layer and Flow Control Vol. 2, pg1166-1349. Pergamon Press, 1961.

[2] Delery, J.M., "Shock Wave/Turbulent Boundary Layer Interaction and its Control," *Prog. Aerospace Sci.*, Vol. 22, 1985, pp. 209-280.

[3] Viswanath, P.R., "Shock-Wave-Turbulent-Boundary-Layer Interaction and its Control: A Survey of Recent Developments," *Sadhana*, Feb., 1988, pp. 45-104.

[4] Bushnell, D. M., "Shock Wave Drag Reduction," *Annual Review of Fluid Mechanics*, Vol. 36, 2004, pp. 81-96.

[5] Ferri A., "Experimental Results with Airfoils Tested in the High-Speed Tunnel at Guidonia", *Atti. Di Godonia*, No. 17, 1939, Eng. Trans. 1940.

[6] Liepmann, H.W., "Interaction between boundary layer and shock waves in transonic flow," *Journal of Aeronautical Sciences,* Vol. 13, 1946, pp. 623-637.

[7] Ackeret, J., Feldmann, F., and Rott, K., "Investigations of Cornpression Shocks and Boundary Layers in Gases Moving at High Speed," NACA TM 1113, 1947.

[8] Liepmann, H.W.; Roshko, A.; and Dhawan, S., "On reflection of shock waves from boundary layers," *National Advisory Committee for Aeronautics*, Report 1100, 1951, pp. 889-917.

[9] Adamson, T.C. Jr. and Messiter, A.F., "Analysis of Two-Dimensional Interactions Between Shock Waves and Boundary Layers," *Annual Review of Fluid Mechanics*, Vol. 12, 1980, pp. 103-138.

[10] Andreopoulos, J. and Muck, K.-C., "Some New Aspects of the Shock-Wave/Boundary-Layer Interaction in Compression-Ramp Flows," *Journal of Fluid Mechanics*, Vol. 180, 1987, pp. 405-428.

[11] Pearcy, HH. Holder, DW. "Examples of the Effects of Shock-Induced Boundary Layer separation in Transonic Flight." *Ministry of Technology*, ARC, R&M No. 3510. January 1954.

[12] Dolling, D.S., "Fifty Years of Shock-Wave/Boundary-Layer Interaction Research: What Next?," *AIAA Journal*, Vol. 39, No. 8, 2001, pp. 1517-1531.

[13] Lin, J.C., "Review of research on low-profile vortex generators to control boundary-layer separation," *Progress in Aerospace Sciences*, Vol. 38, 2002, pp. 389-420.

[14] Ashill, P.R., Fulker, J.L., and Hackett, K.C., "Research at DERA on Sub Boundary Layer Vortex Generators (SBVGs)," AIAA Paper AIAA-2001-0887, Jan, 2001.

[15] Barter, J.W., Dolling, D.S., "Experimental Study of the Use of Vortex Generators to Reduce Fluctuating Pressure Loads in Shock Wave Turbulent Boundary Layer Interactions." AIAA Paper AIAA-1993-4335, Oct, 1993.

[16] Stanewsky, E., Delery, J.; Fulker, J.; Matteis, P. de (Editors). "Drag Reduction by Shock and Boundary Layer Control", Springer, 2002.

[17] Holden, H. and Babinsky, H., "Effect of Microvortex Generators on Separated Normal Shock/Boundary Layer Interactions," *Journal of Aircraft*, Vol. 44, No.1, 2007, pp. 170-174.

[18] Lee, S., Loth, E., and Babinsky, H., "Normal Shock Boundary Layer Control with Various Vortex Generator Geometries," *Computers and Fluids*, Vol. 49, 2011, pp. 233-246.

[19] Gordeyev, S., Burns, R., Jumper, E., Gogineni, S, Paul, M., and Wittich, D., "Aero-Optical Mitigation of Shocks Around Turrets at Transonic Speeds Using Passive Flow Control", AIAA Paper AIAA-2013-0717, Jan 2013.

[20] Wallis, R.A., Stuart, C.M. "On the Control of Shock-Induced Boundary-Layer Separation with Discrete Air Jets." *Ministry of Aviation Aeronautical Research Council.* C.P. No. 595, February, 1958.

[21] Englar, Robert J. "Two-Dimensional Transonic Wind Tunnel Tests of Three 15-percent Thick Circulation Control Airfoils." NSRDC, Technical Note AL-182, December 1970.

[22] Krogmann, P., Stanewsky, E., and Thiede, P., "Effects of Suction on Shock/Boundary-Layer Interaction and Shock-Induced Separation," *Journal of Aircraft*, Vol. 22, No.1, 1985, pp. 37-42.

[23] Souverein, L.J. and Debieve, J.-F., "Effect of Air Jet Vortex Generators on a Shock Wave Boundary Layer Interaction," *Experiments in Fluids*, Vol. 49, 2010, pp. 1053-1064.

[24] Kalra, C.S, Shneider, M.N., and Miles, R.B., "Numerical Study of Boundary Layer Separation Control Using Magnetogasdynamic Plasma Actuators," *Physics of Fluids*, Vol. 21, 2009, 106101.

[25] Kalra, C.S, Zaidi, S.H., Miles, R.B., and Macheret, S.O., "Shockwave–Turbulent Boundary Layer Interaction Control Using Magnetically Driven Surface Discharges," *Experiments in Fluids*, Vol. 50, 2011, 547-559.

[26] Narayanaswamy, V., Clemens, N.T., and Raja, L.L., "Investigation of a Pulsed-Plasma Jet for Shock / Boundary Layer Control," AIAA Paper 2010-1089, Jan, 2010.

[27] Babinsky, Holger. Harvey, John K. "Shock Wave-Boundary-Layer Interactions," Cambridge University Press, 2011.

[28] Vukasinovic, B. Gissen, A.N., Glezer, A., and Gogineni, S. "Fluidic Control of Transonic Shock-Induced Separation," AIAA Paper AIAA-2013-0529.

American Institute of Aeronautics and Astronautics